sustainability

MDPI

Article

Carbene Ligand-Doped Fe_2O_3 Composite for Rapid Removal of Multiple Dyes under Sunlight

Siwei Yang [1,†], Yichao Zhuang [1,†], Yuanfang Shen [1], Weihang Han [1], Liangchen Chen [1], Qiang Sun [2,*], Di Wu [1,*] and Hui Zheng [1,*]

[1] College of Material, Chemistry and Chemical Engineering, Hangzhou Normal University, Hangzhou 311121, China; 2020111009018@stu.hznu.edu.cn (S.Y.); 2019111009031@stu.hznu.edu.cn (Y.Z.); 2019111009018@stu.hznu.edu.cn (Y.S.); 2020112009033@stu.hznu.edu.cn (W.H.); 2020111009011@stu.hznu.edu.cn (L.C.)

[2] Australian Research Council Centre of Excellence for Nanoscale BioPhotonics (CNBP), School of Science, RMIT University, Melbourne, VIC 3001, Australia

* Correspondence: qiang.sun@rmit.edu.au (Q.S.); wudi2007@126.com (D.W.); huizheng@hznu.edu.cn (H.Z.); Tel.: +86-571-28861932 (H.Z.)

† Equal author contributions.

Abstract: Contaminated water due to industrial organic dyes presents a significant challenge to sustainability. As a material of green energy, photocatalysts offer an effective and environmentally friendly way to deal with organic dyes for water treatment. A series of simple and highly efficient iron photocatalysts with carbene ligands were developed, which, under the illumination of sunlight, can rapidly degrade multiple organic dyes in water at room temperature, including rhodamine B (RhB), indigo carmine (IC), methyl blue (MB), and congo red (CR). The field-only surface integral method was carried out to determine the absorption spectrum of photocatalyst particles. Under the optimized experimental conditions which were selected by the orthogonal experiments for four dyes, 0.5a@Fe_2O_3 and 2c@Fe_2O_3 demonstrated good stability and photocatalytic activity. These two composite materials not only have the ability to remove 98.0% of the degradation in 10 s, but also maintain high reactivity after a few cycles of repeated use.

Keywords: wastewater; organic dyes; carbene; iron photocatalyst; adsorption; simulation calculations

check for updates

Citation: Yang, S.; Zhuang, Y.; Shen, Y.; Han, W.; Chen, L.; Sun, Q.; Wu, D.; Zheng, H. Carbene Ligand-Doped Fe_2O_3 Composite for Rapid Removal of Multiple Dyes under Sunlight. *Sustainability* **2021**, *13*, 12669. https://doi.org/10.3390/su132212669

Academic Editor: Agostina Chiavola

Received: 9 October 2021
Accepted: 9 November 2021
Published: 16 November 2021

Publisher's Note: MDPI stays neutral with regard to jurisdictional claims in published maps and institutional affiliations.

Copyright: © 2021 by the authors. Licensee MDPI, Basel, Switzerland. This article is an open access article distributed under the terms and conditions of the Creative Commons Attribution (CC BY) license (https://creativecommons.org/licenses/by/4.0/).

1. Introduction

Though our planet has abundant freshwater resources, they are far from inexhaustible and are not evenly distributed. The global water quality deterioration is a severe challenge to our sustainability. The growth of the world population, the acceleration of urbanization and the expansion of industry and agriculture not only consume a lot of freshwater but also pollute the limited freshwater resources, which worsens the living environment of human beings. In developing countries, only around 5% of industrial and domestic wastewater is treated [1], while most of the rest, which contains toxic and dangerous by-products of industrial production, is directly discharged without treatment. This leads to the serious pollution of soil, rivers, and groundwater. Indeed, the discharge of untreated dye wastewater is a major factor for natural water pollution [2]. The main hazards of dye wastewater are as follows: the chromaticity of dyes in wastewater can absorb light, reduce the transparency of water, consume a large amount of oxygen in water [3], and promote the growth of aquatic organisms and microorganisms. Additionally, most dyes are aromatic azo compounds [4]. When the biological toxicity is relatively high, some of them can even cause mutagenesis, carcinogenesis, and teratogenesis [5]. Moreover, since heavy metals in dye wastewater are not biodegradable, they can continue to be taken in through the food chain to accumulate in human bodies, which leads to diseases such as diarrhea, cholera, dysentery, typhoid, and polio [6]. The high content of organic matter in water, such as urea,

is often derived from various processes of printing and dyeing, which increase the content of total phosphorus and nitrogen in wastewater and leads to water eutrophication [7–9]. If the dye wastewater is discharged directly without treatment, it will pose a great threat to the increasingly limited source of drinking water. Therefore, the treatment of wastewater is critical to reducing environmental pollution to protect human health and to save freshwater resources, which is important for our sustainable development [10,11].

At present, a significant amount of research work has been conducted on the treatment of wastewater. The main methods used include physical methods, chemical methods, biological methods, and the combination of these methods. Physical methods normally use activated carbon [12–14] and resin adsorbents [15–18], and the decolorization mechanism mainly includes adsorption and ion exchange [19]. This method is effective and easy to operate, and is one of the most mature methods to treat dye wastewater. However, a disadvantage of physical methods is that each adsorbent is normally limited to adsorbing a particular type of dye. The commonly used biological methods include the activated sludge method, the biofilm method, and the anaerobic biological method [20–22]. A disadvantage of these methods is that adsorbents are limited to adsorbing the specified dyes. Chemical methods to treat dye wastewater use chemical reactions to separate and recycle pollutants in wastewater or change their properties to make the water harmless. The main methods of dye wastewater treatment [23–25], coagulation [26–28], oxidation [29–32], photochemical [33–37], and electrochemical [38–40] are commonly used in the treatment of azo dye wastewater. Among them, the photochemical method is the most attractive method as it utilizes clean solar energy [41].

A promising photocatalyst [42], the iron-based photocatalyst, has been widely used in the degradation of organic dyes due to its wide light absorption range, low cost, adjustable bandgap, high stability, and recyclability [43]. Iron-based photocatalysts can be categorized into three types, including iron oxide-compounding [44–46], iron ion-doping [47,48] and iron oxide-modifying [43,49,50]. Xiaohui Feng et al. reported a novel kind of Fe_3O_4-ZnO hybrid nanoparticle, which exhibits an outstanding phenol degradation of 82.3% in comparison with ZnO (52%) [51]. Ultra-small ZnS:Fe quantum dots were synthesized for the photodegradation of malachite green (MG) with a degradation rate of up to 98% [52]. Ramin Hassandoost modified Fe_3O_4 nanoparticles with Ce^{3+}/Ce^{4+} and doped the nanoparticles onto graphene oxide sheets for the decontamination of oxytetracycline [53].

In the field of metal-organic catalysis, carbenes, with good δ-electron-donating and π-electron-withdrawing abilities, are mainly used as ligands to form strong bonds with transitional metals [54–57]. Carbenes, especially N-heterocyclic carbenes (NHCs), are easy to prepare and can easily adjust the steric hindrance and electronic effects, depending on the modification of the substituents on the nitrogen atom [58–61]. The metal–carbene complexes can provide high activity and good stability in catalytic reactions [62–65]. The addition of carbene can transfer photogenerated electron–hole pairs in a directional direction, thereby improving the utilization of electrons [66]. In this paper, we revealed that a composite photocatalyst, carbene-doped Fe-based metal Xa@Fe_2O_3, can be well excited to generate electron–hole pairs with a prolonged lifetime of photogenerated electrons. By switching different ligands, the morphology of photocatalyst particles can be controlled to further regulate the light absorption performance. Thus, Xa@Fe_2O_3 materials can potentially be used as photocatalysts to treat wastewater with organic dye pollutants. In the next section, the preparation of carbene ligands and the synthesis of Xa@Fe_2O_3 are demonstrated. The characterization, photophysical properties, and photocatalytic mechanics and performance of Xa@Fe_2O_3 are described and discussed in Section 3. Then, some concluding remarks are given in Section 4.

2. Materials and Methods

2.1. Preparation of Photocatalysts

2.1.1. Preparation of Ligands

Three ligands, a, b, and c, were prepared by the authors according to the literature [67]. The synthetic process and ligand structures are shown in Figure 1.

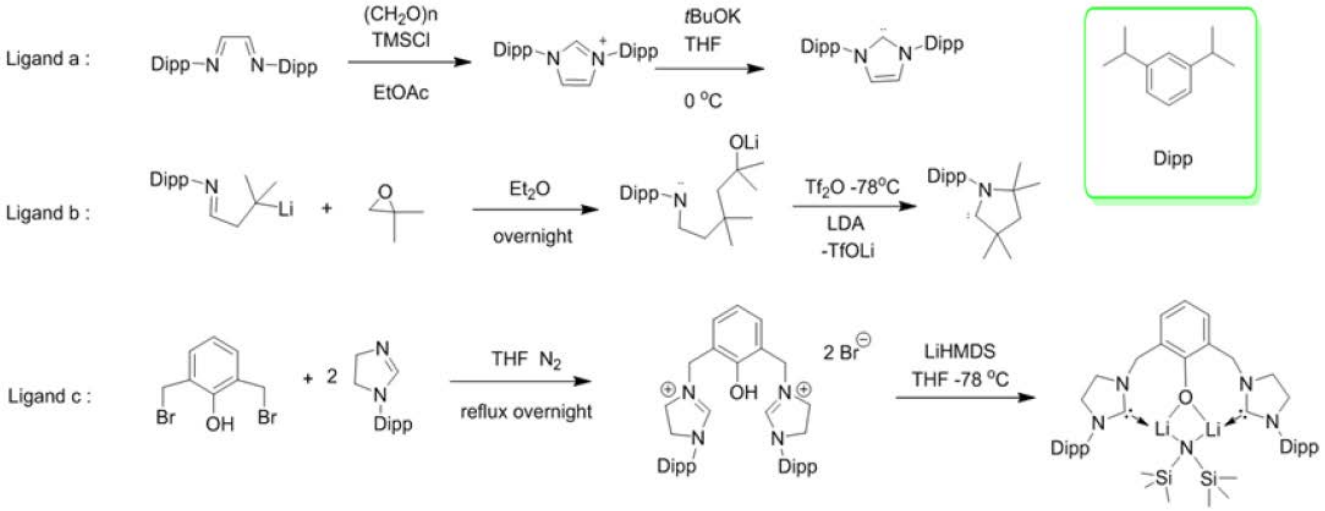


Figure 1. Synthesis of three ligands.

2.1.2. Preparation of Composite Catalyst

A series of photocatalysts were fabricated using a direct solvothermal method. Different equivalents of ligand-a were added to a 10 mL mixed solution that contains DMF and EtOH (V:V = 1:1). After stirring for 10 min, $FeCl_3$ (2 mmol) was added to the mixed solution and stirred for 10 more minutes. The solution was transferred to a Teflon-lined stainless steel autoclave and put into a drying oven at 200 °C. After heating for 15 h and then cooling to room temperature, the resulting mixture was filtered and the solid was washed with DMF (7 mL) and EtOH (7 mL) three times, respectively. Finally, the solid was dried at 80 °C in a vacuum drying oven for 12 h. The prepared sample was named Xa@Fe_2O_3, where X represents the molar ratio of the ligand to the iron salt. As a result, 0.5a@Fe_2O_3, 1a@Fe_2O_3, and 2a@Fe_2O_3 were obtained. Xb@Fe_2O_3 and Xc@Fe_2O_3 were synthesized in the same way but by using different ligands. Fe_2O_3 with no ligand was also synthesized in the same manner for comparison. In the ^{13}C NMR spectra of Ligand-c, presumably due to the coupling with lithium atoms, the signal for the carbene atoms directly bonding to boron atoms could not be observed.

2.1.3. Characterization

All synthesis reactions were carried out under the atmospheric pressure of dry argon using standard Schlenk or dry box technology. The structure of N-carbene organic ligand was confirmed by NMR spectroscopy (Bruker Co., Ltd., Karlsruhe, Germany, Avance 500 MHz). Melting points were measured with BUCHI Labortechnik AG (BUCHI Co., Ltd., Zurich, Switzerland). XRD (Bruker Co., Ltd., Karlsruhe, Germany, Bruker D8 Advance) patterns were recorded with the Smart lab 9 kw advance powder X-ray Cu Ka radiation diffractometer (40 kV, 40 mA, λ = 1.54056 Å). The XPS (Thermo Co., Ltd., Waltham, MA, USA) measurements were performed in the Thermo Scientific K-Alpha spectrometer (12 KV, 6 mA). The SEM (Zeiss Co., Ltd., oberkochen, Germany) was carried out on the Zeiss Sigma 300 (1.0 kV, 1.6 nm). The specific surface area BET test (Micromeritics instrument Ltd., Atlanta, GA, USA) was used to detect the specific surface area of the catalyst. Electron spin resonance (ESR) analyses were conducted using the Bruker EMXPLUS spectrometer (Bruker Co., Ltd., Karlsruhe, Germany) at room temperature using DMPO (5,5-dimethyl-1-

pyrroline Noxide) as a radical scavenger of superoxide radical O^{2-} and hydroxyl radical OH. Electrochemical impedance spectroscopy (EIS) tests were carried out in a 2.5 mmol L^{-1} $K_3[Fe(CN)_6]$ aqueous electrolyte by CHI 760E (NBeT Co., Ltd., Beijing, China), which was equipped with a 10 mv sinusoidal AC voltage and a 300 W xenon lamp source (>420 nm, CEAuLight Co., Ltd., Beijing, China).

2.1.4. Photocatalytic Measurements

Rhodamine B (RhB), methyl blue (MB), indigo carmine (IC), and congo red (CR) were used as degradation models to assess the photocatalytic activities of three photocatalysts. As in a typical experimental process, a certain amount of catalyst particles was added into a 5 mL organic dye solution. Then, 1 mL of the reaction solution was extracted at a specific time, after which the catalyst particles were removed by a needle filter (0.22 μm, 13 mm, Titan), and the degradation of the organic dye was measured with a UV–Vis spectrometer (Shanghai Jinghua Technology Instrument Co., Ltd., Shanghai, China). For the recycling experiments, the photocatalyst particles were centrifuged and dried for the next experiment. A Newport solar simulator (500 W, 94023A, Newport Co., Ltd., Irvine, CA, USA) was used as the light source to simulate sunlight.

3. Results and Discussion

3.1. Structure and Characterization

The morphologies of the as-prepared samples were characterized by SEM. Figure 2a–d correspond to the catalysts, pure Fe_2O_3, 0.5a@Fe_2O_3, 2b@Fe_2O_3, and 2c@Fe_2O_3, respectively. The addition of ligands would have a corresponding impact on the morphology and structure of the catalysts and on the final degradation. 2a@Fe_2O_3 is in the form of small particles. Due to its small particle size, it has a large surface area and a good degradation effect. 2b@Fe_2O_3 presents a large mass, and it has no degradation activity, which may be related to the specific surface area. 2c@Fe_2O_3 is thin-layered and has a good degradation effect.

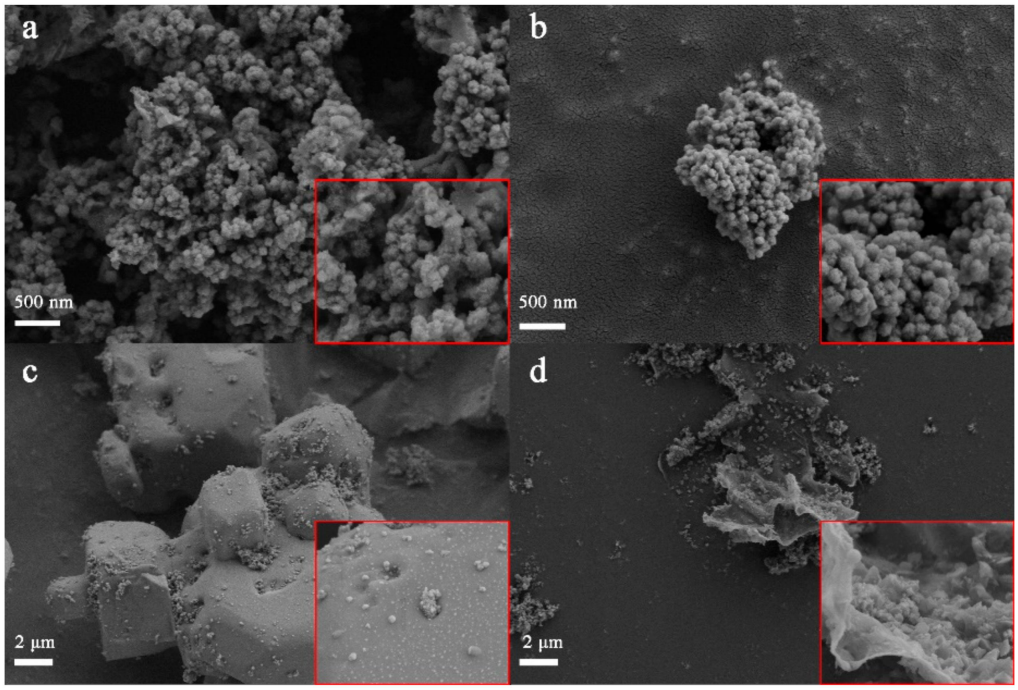


Figure 2. SEM of (**a**) pure Fe_2O_3, (**b**) 0.5a@Fe_2O_3, (**c**) 2b@Fe_2O_3 and (**d**) 2c@Fe_2O_3.

Taking 0.1a@Fe_2O_3 as an example, the specific surface area of the catalyst was measured, and the nitrogen adsorption and desorption equilibrium isotherm curve was obtained (Figure 3a). It was concluded that the catalyst surface area was 49.7419 m^2/g, and

the Langmuir surface area was 236.0050 m^2/g. The internal structure of the catalyst was basically non-porous. The phase structures of as-synthetized Fe_2O_3, 0.5a@Fe_2O_3, and 2c@Fe_2O_3 were characterized by XRD analyses. A series of corresponding Fe_2O_3 (JCPDS card umber 33-0664) (0 1 2), (1 0 4), (1 1 0), (1 1 3), (0 2 4), (1 1 6), (2 1 4), and (3 0 0) plane diffraction peaks can be observed at 24.1°, 33.1°, 35.6°, 40.9°, 49.5°, 54.1°, 62.4°, and 64.0°, respectively, as shown in Figure 3. The XRD pattern of 2c@Fe_2O_3 showed several new peaks appearing at 21.4°, 30.5°, and 34.1°, which may be related to the ligand. In the hydrothermal process, a small part of Si in the ligand is oxidized by the little amount of dissolved oxygen in the solvent.

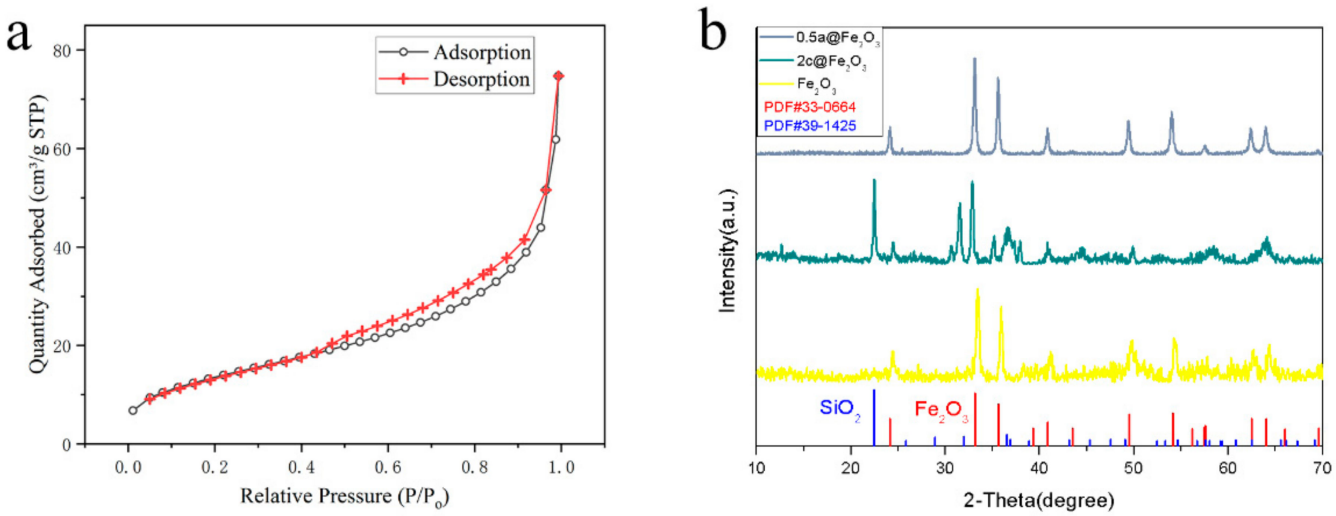


Figure 3. (**a**) N_2 adsorption–desorption isotherms; (**b**) XRD of pure Fe_2O_3, 0.5a@Fe_2O_3 and 2c@Fe_2O_3.

The XPS analyses were carried out to confirm that the ligands were doped on Fe_2O_3. Figure 4a,c show the survey scan of XPS spectra for 0.5a@Fe_2O_3 and 2c@Fe_2O_3, respectively. The five peaks at 55.3, 283.7, 399.9, 530.3, and 711.0 eV correspond to the Li1s, C1s, N1s, O1s, and Fe2p, respectively, signifying the success of the ligand dope. The VB values of 0.5a@Fe_2O_3 and 2c@Fe_2O_3 were 1.32 eV and 0.85 eV, respectively, according to the VB-XPS spectra, as shown in Figure 4b,d.

3.2. Photophysical Properties

As shown in Figure 5, the plots of $(\alpha hv)^2$ along with photon energy (hv) for 0.5a@Fe_2O_3 and 2c@Fe_2O_3 were used to calculate the Eg of these two photocatalysts, which turned out to be 1.99 eV and 1.80 eV, respectively. According to the formula $E_{CB} = E_{VB} - E_g$, the E_{CB} of 0.5a@Fe_2O_3 and 2c@Fe_2O_3 were −0.67 eV and −0.95 eV, respectively.

To confirm the efficiency of as-synthesized photocatalysts in preventing the recombination of photogenerated electron–hole pairs, the results of EIS in Figure 6 show that 0.5a@Fe_2O_3 has the smallest arc size, which means it has the least electron transfer resistance. Analogously, 0.5a@Fe_2O_3 and 2c@Fe_2O_3 have a better charge separation efficiency when compared to 2b@Fe_2O_3, which is consistent with the results of the degradation experiments.

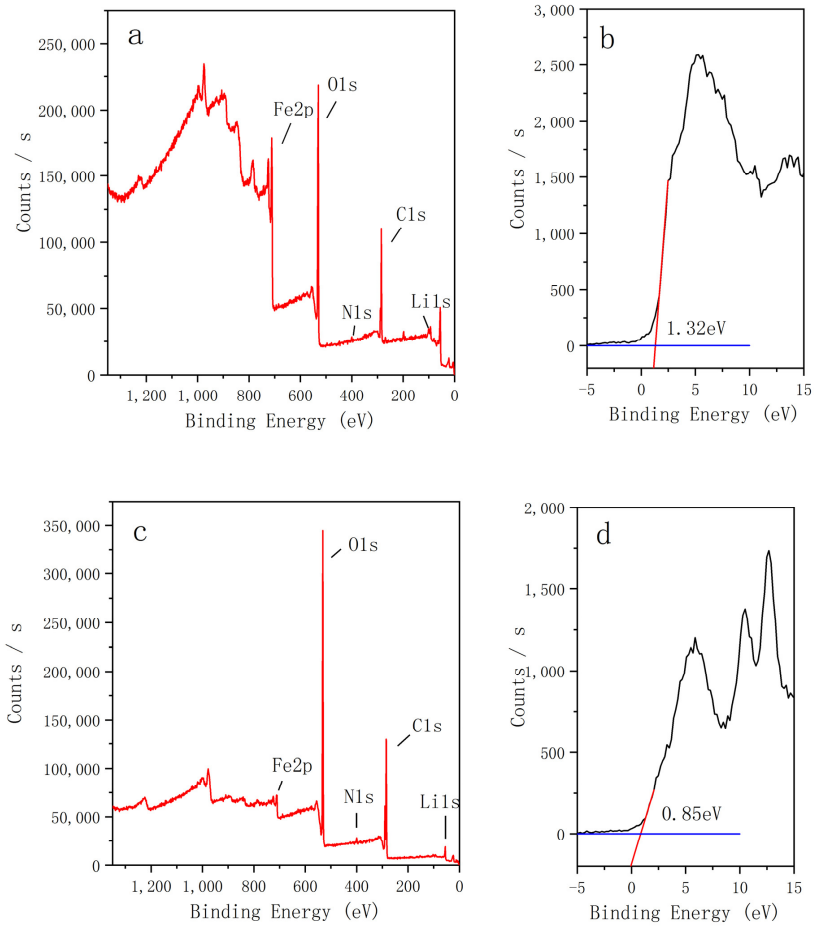


Figure 4. XPS of (**a**) 0.5a@Fe_2O_3 and (**c**) 2c@Fe_2O_3; XPS-VB of (**b**) 0.5a@Fe_2O_3 and (**d**) 2c@Fe_2O_3.

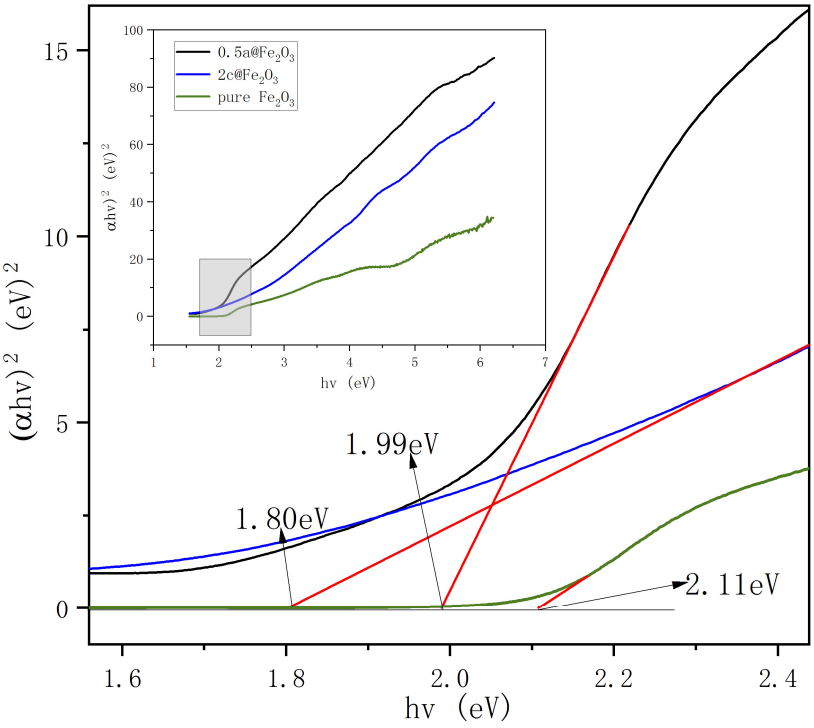


Figure 5. Plots of $(\alpha hv)^2$ versus photon energy (hv) for the band gap energies of pure Fe_2O_3, 0.5a@Fe_2O_3 and 2c@Fe_2O_3.

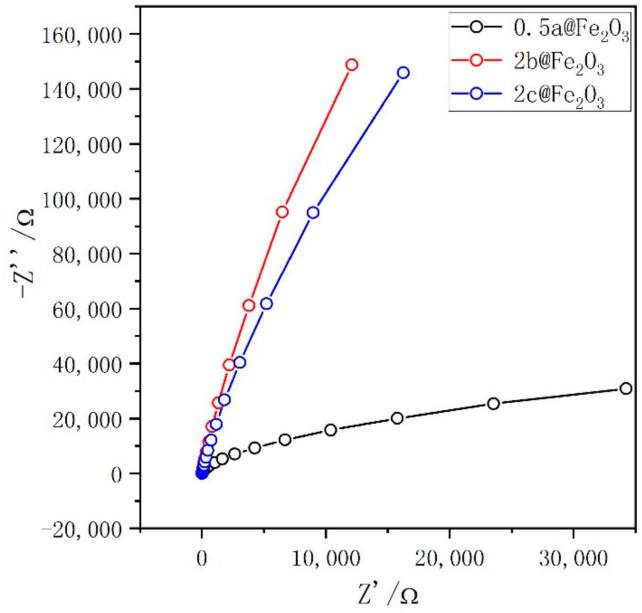


Figure 6. EIS Nyquist plots of 0.5a@Fe_2O_3, 2b@Fe_2O_3 and 2c@Fe_2O_3.

3.3. Photophysical Mechanism

To further confirm the main active species, the ESR experiments for 0.5a@Fe_2O_3 and 2c@Fe_2O_3 were carried out in the dark and under irradiation, respectively. The characteristic signals of DMPO-·OH and DMPO-·O_2^- can be clearly observed in Figure 7, indicating that both ·OH and ·O_2^- were present in the photodegradation. The difference is the main free radicals in the degradation process; the superoxide radical was used for 2c@Fe_2O_3 and 0.5a@Fe_2O_3 was dominated by the hydroxyl radical.

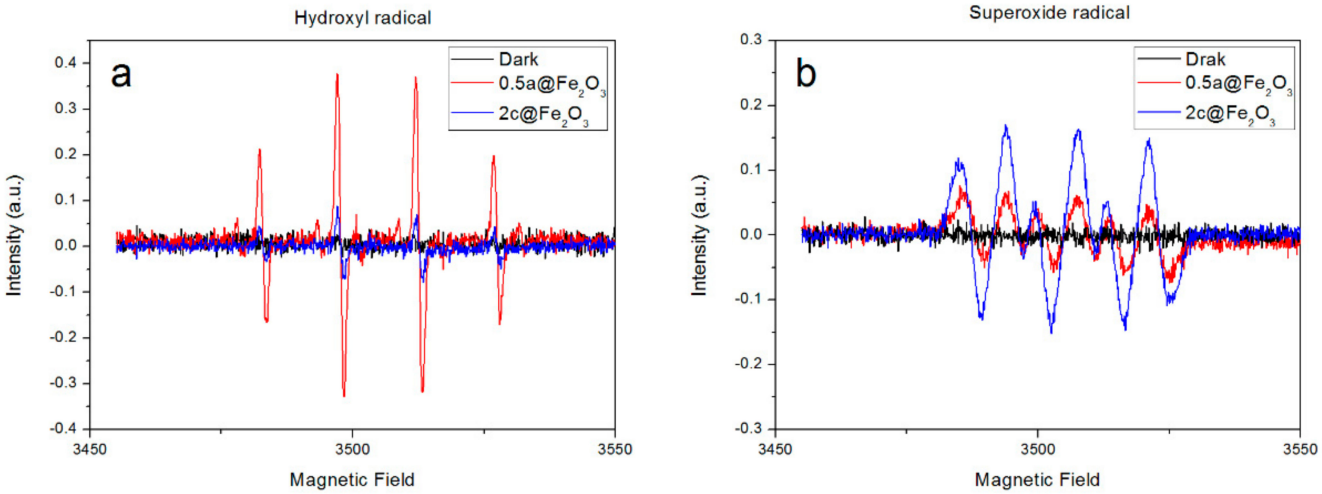


Figure 7. ESR spectra of the (**a**) DMPO-·OH and (**b**) DMPO-O_2^- for 0.5a@Fe_2O_3 and 2c@Fe_2O_3 under same irradiation time.

3.4. Absorption Spectrum

As shown in the SEM images in Figure 2, an obvious difference between 0.5a@Fe_2O_3 and 2c@Fe_2O_3 is that 0.5a@Fe_2O_3 is a 3D spherical particle while 2c@Fe_2O_3 is a layer ellipsoidal particle. Such a geometric difference alters the interactions between light and particles, in particular the light absorption, which in turn can affect the photocatalytic performance. To study the geometric effects, we calculated the light absorption spectra of 0.5a@Fe_2O_3 and 2c@Fe_2O_3 in water by using the field-only surface integral method [68–71].

As displayed in the insets of Figure 8, the visible light is represented by a plane wave propagating along the k_0 direction, where $|k_0| = k = 2\pi/\lambda$ is the wavenumber and λ the wavelength. The water refractive index is n_{water} = 1.33, and the refractive index of Fe_2O_3 was obtained from the literature [72]. The 0.5a@Fe_2O_3 particle is represented by a sphere with a diameter of 0.8 µm. The 2c@Fe_2O_3 particle is represented by an ellipsoid as $x^2/a^2 + y^2/b^2 + z^2/c^2 = 1$ with $2a = 6$ µm, $b/a = 0.11$ and $c/a = 0.33$.

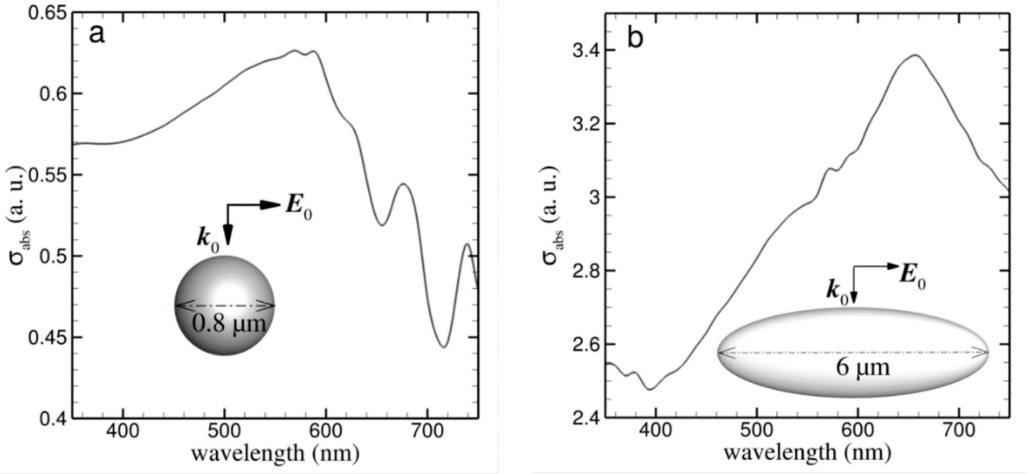


Figure 8. Spectrum of absorption cross sections of (**a**) a spherical 0.5a@Fe_2O_3 particle and (**b**) an ellipsoid 2c@Fe_2O_3 particle under the illumination of visible light with the wavelengths varying from 350 to 750 nm in a step of 10 nm.

In Figure 8, the absorption cross section, $\sigma_{abs} = 1/2 \int_S Real[E \times H^*] \cdot dS$, is shown, where E and H are the electric and magnetic fields in water, respectively, a superscript $*$ indicates the conjugate of the field values, and S is a surface that encloses the particle. Comparing the spectrum of σ_{abs} for 0.5a@Fe_2O_3 in Figure 8a to that of 2c@Fe_2O_3 in Figure 8b, the peak absorption wavelength of 0.5a@Fe_2O_3 is at 590 nm (2.10 eV) while that of 2c@Fe_2O_3 is at 660 nm (1.89 eV). The shift of the peak absorption light wavelength might contribute to the photocatalytic effectiveness of these two types of particles on different dyes.

3.5. Photocatalytic Degradation Performances

Orthogonal experiments were carried out to find the optimum combination of condition levels for the degradation experiments. Four variables at three levels were investigated, including the concentration of dye solution (A), the molar ratio of ligand to ferric salt (B), the types of ligands (C), and the catalyst dosage (D). The optimization table of photodegradation is shown in Tables 1–3. Four kinds of dyes (RhB, CR, MB, and IC) were chosen to represent the organic pollutants in wastewater.

Table 1. Optimization table of photodegradation.

Entry	A/mg·L^{-1}	B	C	D/mg [a]
1	5	0.5	a	1
2	10	1	b	4
3	20	2	c	7

[a] Centrifugation operation was carried out in recycle experiments. After centrifugation, the catalyst was collected and dried in the original tube; then, it was employed again in the same tube in next run.

Table 2. The results of the orthogonal experimental.

	Factors				Degradation Rate in 1 h/%			
Entry	**A**	**B**	**C**	**D**	**RhB**	**CR**	**MB**	**IC**
1	1	1	1	1	66.7	14.9	55.6	78.7
2	1	2	2	2	83.8	21.1	67.9	54.1
3	1	3	3	3	100.0	99.0	97.5	67.6
4	2	1	2	3	68.0	54.8	82.9	88.9
5	2	2	3	1	97.8	94.7	98.9	27.5
6	2	3	1	2	89.1	90.9	96.6	93.1
7	3	1	3	2	98.9	99.5	100.0	99.6
8	3	2	1	3	43.9	11.8	84.3	92.0
9	3	3	2	1	47.0	97.8	76.4	43.6

Table 3. Range analysis of orthogonal experimental results.

K/%	**Dyes**	**A/mg·L^{-1}**	**B**	**C**	**D/mg**
K_1	RhB	83.5	77.9	66.6	70.5
	CR	45.0	56.4	39.2	69.1
	MB	73.7	79.5	78.8	77.0
	IC	66.8	89.1	87.9	49.9
K_2	RhB	85.0	75.2	66.3	90.6
	CR	80.1	42.5	57.9	70.5
	MB	92.8	83.7	75.7	88.2
	IC	69.8	57.9	62.2	82.3
K_3	RhB	63.3	78.7	98.9	70.6
	CR	69.7	95.9	97.7	55.2
	MB	86.9	90.2	98.8	88.2
	IC	78.4	68.0	64.9	82.8
R	RhB	20.2	3.5	32.6	20.1
	CR	35.1	53.4	58.5	15.2
	MB	19.1	10.7	23.1	11.2
	IC	11.6	21.1	25.7	32.9

Based on the numerical calculation results, the optimal combinations of degradation for four dyes (RhB, CR, MB, and IC) were determined as A2B3C3D2, A2B3C3D2, A2B3C3D3, and A3B1C1D3, respectively. To confirm the optimal combination, a series of degradation experiments were performed on these four sets of combinations. As shown in Figure 9, all of them can be reduced by 98.0% within 10 s, showing the good degradation ability of the catalyst. Figure 10 presents the cycle experiments of the photocatalyst towards four dyes, which shows that the stability and reusability of 0.5a@Fe_2O_3 and 2c@Fe_2O_3 for different dyes. After five cycles, the degradation of RhB by 2c@Fe_2O_3 and IC by 0.5a@Fe_2O_3 remain efficient, while for MB and CR, the degradation ability of 2c@Fe_2O_3 decreases gradually. Compared with the same catalyst, some dyes are easier to degrade than others. This has a significant relationship with the chemical structure of the dye. Taking Rhodamine B as an example, the molecule of RhB is more polar and easily adsorbed on the surface of the catalyst. The photogenerated electron–hole pairs can be used directly and effectively, thereby improving the photocatalytic efficiency. If the dye has a weak polarity and is easy to disperse in the solution, some electrons will be annihilated [73].

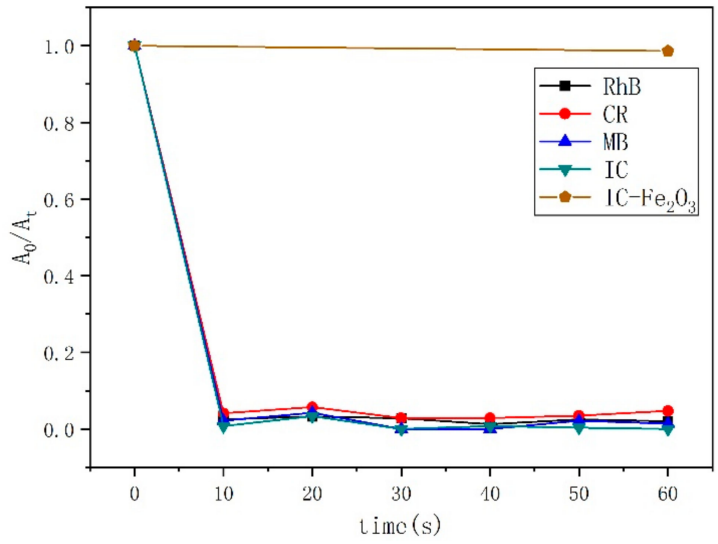


Figure 9. The degradation curve of four dyes on the respective optimum conditions (A2B3C3D2 for RhB, A2B3C3D2 for CR, A2B3C3D3 for MB, A3B1C1D3 for IC).

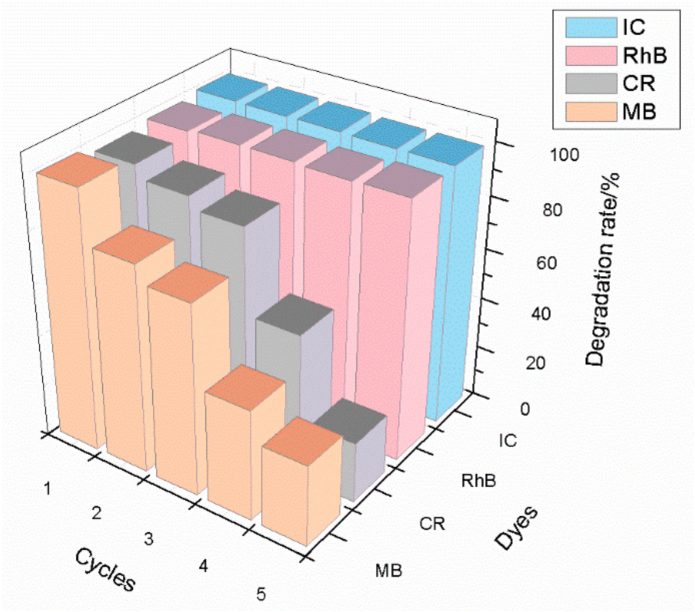


Figure 10. Cycle experiment of four dyes under respective optimum conditions (A2B3C3D2 for RhB, A2B3C3D2 for CR, A2B3C3D3 for MB, A3B1C1D3 for IC).

4. Conclusions

In summary, we have successfully synthesized a series of iron-based photocatalysts with carbene ligands which demonstrate good photocatalytic capabilities to degrade RhB, CR, MB, and IC under the illumination of sunlight. The electronic effect between the carbene and Fe_2O_3 hinders the electron–hole pair recombination rate, which has been confirmed as the photocatalytic mechanics of the synthesized carbene-doped Fe_2O_3. All dyes can be degraded quickly in ten seconds under the optimal conditions which were obtained based on orthogonal experiments. The light absorption spectra of photocatalysts in water were calculated to study the geometric effects; the results showed good absorptions in the visible region. Consequently, as an effective and efficient photocatalytic material, carbene-doped Fe_2O_3 is expected to open new means of environmental remediation.

Author Contributions: Experiment and writing, S.Y.; experiment and formal analysis, Y.Z.; data curation Y.S.; visualization, W.H.; formal analysis, L.C.; theoretical calculation and modeling software, Q.S.; formal analysis and resources, D.W.; idea, design, modification, and methodology, H.Z. All authors have read and agreed to the published version of the manuscript.

Funding: This research was funded by National Natural Science Foundation of China (21978061), Zhejiang Provincial Natural Science Foundation of China (LY19B060007, LQ20B010007), Discovery Early Career Researcher Award (DE150100169) and Centre of Excellence Grant (CE140100003) by the Australian Research Council (ARC).

Institutional Review Board Statement: This research work did not involve humans or animals.

Informed Consent Statement: Not applicable.

Data Availability Statement: Not applicable.

Acknowledgments: We are thankful to National Natural Science Foundation of China (21978061), Zhejiang Provincial Natural Science Foundation of China (LY19B060007, LQ20B010007) and Zhejiang Key Laboratory of Green Pesticides and Cleaner Production Technology for providing financial support. Q.S. was supported by the Australian Research Council (ARC) through Discovery Early Career Researcher Award (DE150100169) and Centre of Excellence Grant (CE140100003). This research was undertaken with the assistance of resources from the National Computational Infrastructure (NCI Australia), which is NCRIS-enabled and supported by the Australian Government.

Conflicts of Interest: The authors declare no conflict of interest.

References

1. Country Files for SDG 6.3.1 "Proportion of Wastewater Safely Treated". Available online: https://www.who.int/water_sanitation_health/monitoring/coverage/wastewater-country-files/en/ (accessed on 18 January 2021).
2. Ungureanu, N.; Vladut, V.; Voicu, G. Water Scarcity and Wastewater Reuse in Crop Irrigation. *Sustainability* **2020**, *12*, 9055. [CrossRef]
3. Hung, Y.-T.; Aziz, H.A.; Ramli, S.F.; Paul, H.H.; Huhnke, C.R.; Adesanmi, B.M. Chemical waste and allied products. *Water Environ. Res.* **2020**, *92*, 1504–1509. [CrossRef] [PubMed]
4. Sales, H.B.; Menezes, R.R.; Neves, G.A.; Souza, J.J.N.D.; Ferreira, J.M.; Chantelle, L.; Menezes de Oliveira, A.L.; Lira, H.D.L. Development of Sustainable Heterogeneous Catalysts for the Photocatalytic Treatment of Effluents. *Sustainability* **2020**, *12*, 7393. [CrossRef]
5. World Health Organization International Agency for Research on Cancer Carcinogen List. Available online: http://www.sda.gov.cn/WS01/CL1991/215896.html (accessed on 3 January 2018).
6. Diseases and Risks. Available online: https://www.who.int/water_sanitation_health/diseases-risks/en/ (accessed on 18 January 2021).
7. Chan, M.K.; Abdullah, N.; Rageh, E.H.A.; Kumaran, P.; Tee, Y.S. Oxidation of ammonia using immobilised FeCu for water treatment. *Sep. Purif. Technol.* **2021**, *254*, 117612. [CrossRef]
8. Roy, K.; Verma, K.; Vikrant, K.; Goswami, M.; Sonwani, R.; Rai, B.; Vellingiri, K.; Kim, K.-H.; Giri, B.; Singh, R. Removal of Patent Blue (V) Dye Using Indian Bael Shell Biochar: Characterization, Application and Kinetic Studies. *Sustainability* **2018**, *10*, 2669. [CrossRef]
9. Kang, C.-W.; Kolya, H. Green Synthesis of Ag-Au Bimetallic Nanocomposites Using Waste Tea Leaves Extract for Degradation Congo Red and 4-Nitrophenol. *Sustainability* **2021**, *13*, 3318. [CrossRef]
10. Albiss, B.; Abu-Dalo, M. Photocatalytic Degradation of Methylene Blue Using Zinc Oxide Nanorods Grown on Activated Carbon Fibers. *Sustainability* **2021**, *13*, 4729. [CrossRef]
11. Tabana, L.; Tichapondwa, S.; Labuschagne, F.; Chirwa, E. Adsorption of Phenol from Wastewater Using Calcined Magnesium-Zinc-Aluminium Layered Double Hydroxide Clay. *Sustainability* **2020**, *12*, 4273. [CrossRef]
12. Mirzapour, P.; Kamyab Moghadas, B.; Tamjidi, S.; Esmaeili, H. Activated carbon/bentonite/Fe_3O_4 nanocomposite for treatment of wastewater containing Reactive Red 198. *Sep. Sci. Technol.* **2020**, *56*, 2693–2707. [CrossRef]
13. Blachnio, M.; Derylo-Marczewska, A.; Charmas, B.; Zienkiewicz-Strzalka, M.; Bogatyrov, V.; Galaburda, M. Activated Carbon from Agricultural Wastes for Adsorption of Organic Pollutants. *Molecules* **2020**, *25*, 5105. [CrossRef]
14. Boontham, W.; Habaki, H.; Egashira, R. Removal of Phenol from Oil Mill Effluent Using Activated Carbon Prepared from Kernel Shell in Thailand's Palm Industry. *J. Chem. Eng. Jpn.* **2020**, *53*, 682–688. [CrossRef]
15. Jia, Y.; Ding, L.; Ren, P.; Zhong, M.; Ma, J.; Fan, X. Performances and Mechanism of Methyl Orange and Congo Red Adsorbed on the Magnetic Ion-Exchange Resin. *J. Chem. Eng. Data* **2020**, *65*, 725–736. [CrossRef]
16. Rahdar, S.; Rahdar, A.; Ahmadi, S.; Mehdizadeh, Z.; Taghavi, M. Preparation, Physical Characterization and Adsorption Properties of Synthesized Co-Ni-Cr Nanocomposites for Highly Effective Removal of Nitrate: Isotherms, Kinetics and Thermodynamic Studies. *Z. Phys. Chem. Int. J. Res. Phys. Chem. Chem. Phys.* **2020**, *234*, 45–62. [CrossRef]

17. Staudt, J.; Scheufele, F.B.; Ribeiro, C.; Sato, T.Y.; Canevesi, R.; Borba, C.E. Ciprofloxacin desorption from gel type ion exchange resin: Desorption modeling in batch system and fixed bed column. *Sep. Purif. Technol.* **2020**, *230*, 115857. [CrossRef]
18. Wang, X.L.; An, W.L.; Tian, F.; Yang, Y.; Xu, H.X.; Wang, D.; Zhao, X.; Xu, P.-P.; Xu, S.; Wang, Y.Z. Fast microwave-assisted hydrolysis of unsaturated polyester resin into column packing for rapid purifying of dye wastewater. *J. Hazard. Mater.* **2020**, *384*, 121465. [CrossRef]
19. Shamsollahi, Z.; Partovinia, A. Recent advances on pollutants removal by rice husk as a bio-based adsorbent: A critical review. *J. Environ. Manage.* **2019**, *246*, 314–323. [CrossRef] [PubMed]
20. Arumugam, N.; Chelliapan, S.; Kamyab, H.; Thirugnana, S.; Othman, N.; Nasri, N.S. Treatment of Wastewater Using Seaweed: A Review. *Int. J. Environ. Res. Public. Health* **2018**, *15*, 2851. [CrossRef]
21. Bhatia, D.; Sharma, N.R.; Singh, J.; Kanwar, R.S. Biological methods for textile dye removal from wastewater: A review. *Crit. Rev. Environ. Sci. Technol.* **2017**, *47*, 1836–1876. [CrossRef]
22. Mishra, S.; Maiti, A. Applicability of enzymes produced from different biotic species for biodegradation of textile dyes. *Clean Technol. Environ. Policy* **2019**, *21*, 763–781. [CrossRef]
23. Liao, Q.; Rong, H.; Zhao, M.; Luo, H.; Chu, Z.; Wang, R. Interaction between tetracycline and microorganisms during wastewater treatment: A review. *Sci. Total Environ.* **2021**, *757*, 143981. [CrossRef]
24. Shindhal, T.; Rakholiya, P.; Varjani, S.; Pandey, A.; Ngo, H.H.; Guo, W.; Ng, H.Y.; Taherzadeh, M.J. A critical review on advances in the practices and perspectives for the treatment of dye industry wastewater. *Bioengineered* **2021**, *12*, 70–87. [CrossRef] [PubMed]
25. Bui, D.N.; Minh, T.T. Investigation of TNT red wastewater treatment technology using the combination of advanced oxidation processes. *Sci. Total Environ.* **2021**, *756*, 143852. [CrossRef]
26. Ozyurt, B.; Camcioglu, S.; Karatokus, T.; Yuksek, C.; Hapoglu, H. Treatment of sunflower oil industry wastewater by coagulation-flocculation and electro-Fenton methods. *J. Fac. Eng. Archit. Gazi Univ.* **2021**, *36*, 275–290.
27. Ye, H.; Chen, L.; Kou, Y.; How, Z.T.; Chelme-Ayala, P.; Wang, Q.; An, Z.; Guo, S.; Chen, C.; Gamal El-Din, M. Influences of coagulation pretreatment on the characteristics of crude oil electric desalting wastewaters. *Chemosphere* **2021**, *264*, 128531. [CrossRef] [PubMed]
28. Lima Beluci, N.d.C.; Pisano Mateus, G.A.; Miyashiro, C.S.; Homem, N.C.; Gomes, R.G.; Fagundes-Klen, M.R.; Bergamasco, R.; Salcedo Vieira, A.M. Hybrid treatment of coagulation/flocculation process followed by ultrafiltration in TiO_2-modified membranes to improve the removal of reactive black 5 dye. *Sci. Total Environ.* **2019**, *664*, 222–229. [CrossRef]
29. Qi, Y.; Guo, C.; Xu, X.; Gao, B.; Yue, Q.; Jiang, B.; Qian, Z.; Wang, C.; Zhang, Y. Co/Fe and Co/Al layered double oxides ozone catalyst for the deep degradation of aniline: Preparation, characterization and kinetic model. *Sci. Total Environ.* **2020**, *715*, 136982. [CrossRef] [PubMed]
30. Reddy, C.V.; Reddy, I.N.; Ravindranadh, K.; Reddy, K.R.; Shetti, N.P.; Kim, D.; Shim, J.; Aminabhavi, T.M. Copper-doped ZrO_2 nanoparticles as high-performance catalysts for efficient removal of toxic organic pollutants and stable solar water oxidation. *J. Environ. Manage.* **2020**, *260*, 110088. [CrossRef]
31. Rueda-Marquez, J.J.; Levchuk, I.; Ibanez, P.F.; Sillanpaa, M. A critical review on application of photocatalysis for toxicity reduction of real wastewaters. *J. Clean Prod.* **2020**, *258*, 120694. [CrossRef]
32. Wang, Y.; Wang, Y.; Yu, L.; Wang, R.; Zhang, X. Highly effective microwave-induced catalytic degradation of Bisphenol A in aqueous solution using double-perovskite intercalated montmorillonite nanocomposite. *Chem. Eng. J.* **2020**, *390*, 124550. [CrossRef]
33. Feng, Z.; Zeng, L.; Zhang, Q.; Ge, S.; Zhao, X.; Lin, H.; He, Y. In situ preparation of g-C_3N_4/$Bi_4O_5I_2$ complex and its elevated photoactivity in Methyl Orange degradation under visible light. *J. Environ. Sci.* **2020**, *87*, 149–162. [CrossRef]
34. Jiang, L.; Yuan, X.; Zeng, G.; Liang, J.; Wu, Z.; Yu, H.; Mo, D.; Wang, H.; Xiao, Z.; Zhou, C. Nitrogen self-doped g-C_3N_4 nanosheets with tunable band structures for enhanced photocatalytic tetracycline degradation. *J. Colloid Interface Sci.* **2019**, *536*, 17–29. [CrossRef]
35. Kilic, M.Y.; Abdelraheem, W.H.; He, X.; Kestioglu, K.; Dionysiou, D.D. Photochemical treatment of tyrosol, a model phenolic compound present in olive mill wastewater, by hydroxyl and sulfate radical-based advanced oxidation processes (AOPs). *J. Hazard. Mater.* **2019**, *367*, 734–742. [CrossRef]
36. Ahmadi, M.; Motlagh, H.R.; Jaafarzadeh, N.; Mostoufi, A.; Saeedi, R.; Barzegar, G.; Jorfi, S. Enhanced photocatalytic degradation of tetracycline and real pharmaceutical wastewater using MWCNT/TiO_2 nano-composite. *J. Environ. Manag.* **2017**, *186*, 55–63. [CrossRef]
37. Natarajan, S.; Bajaj, H.C.; Tayade, R.J. Recent advances based on the synergetic effect of adsorption for removal of dyes from waste water using photocatalytic process. *J. Environ. Sci.* **2018**, *65*, 201–222. [CrossRef] [PubMed]
38. Xia, Y.; Wang, G.; Guo, L.; Dai, Q.; Ma, X. Electrochemical oxidation of Acid Orange 7 azo dye using a PbO_2 electrode: Parameter optimization, reaction mechanism and toxicity evaluation. *Chemosphere* **2020**, *241*, 125010. [CrossRef] [PubMed]
39. Bian, X.; Xia, Y.; Zhan, T.; Wang, L.; Zhou, W.; Dai, Q.; Chen, J. Electrochemical removal of amoxicillin using a Cu doped PbO_2 electrode: Electrode characterization, operational parameters optimization and degradation mechanism. *Chemosphere* **2019**, *233*, 762–770. [CrossRef]
40. Li, X.; Tang, S.; Yuan, D.; Tang, J.; Zhang, C.; Li, N.; Rao, Y. Improved degradation of anthraquinone dye by electrochemical activation of PDS. *Ecotoxicol. Environ. Saf.* **2019**, *177*, 77–85. [CrossRef]

41. Kaur, R.; Kaur, H. Solar Driven Photocatalysis—An Efficient Method for Removal of Pesticides from Water and Wastewater. *Biointerface Res. Appl. Chem.* **2021**, *11*, 9071–9084.
42. Lebogang, L.; Bosigo, R.; Lefatshe, K.; Muiva, C. Ag_3PO_4/nanocellulose composite for effective sunlight driven photodegradation of organic dyes in wastewater. *Mater. Chem. Phys.* **2019**, *236*, 121756. [CrossRef]
43. Hitam, C.N.C.; Jalil, A.A. A review on exploration of Fe_2O_3 photocatalyst towards degradation of dyes and organic contaminants. *J. Environ. Manage.* **2020**, *258*, 110050. [CrossRef] [PubMed]
44. Gao, S.; Guo, C.; Hou, S.; Wan, L.; Wang, Q.; Lv, J.; Zhang, Y.; Gao, J.; Meng, W.; Xu, J. Photocatalytic removal of tetrabromobisphenol A by magnetically separable flower-like BiOBr/BiOI/Fe_3O_4 hybrid nanocomposites under visible-light irradiation. *J. Hazard. Mater.* **2017**, *331*, 1–12. [CrossRef]
45. Li, B.; Meng, M.; Cui, Y.; Wu, Y.; Zhang, Y.; Dong, H.; Zhu, Z.; Feng, Y.; Wu, C. Changing conventional blending photocatalytic membranes (BPMs): Focus on improving photocatalytic performance of Fe_3O_4/g-C_3N_4/PVDF membranes through magnetically induced freezing casting method. *Chem. Eng. J.* **2019**, *365*, 405–414. [CrossRef]
46. Wang, J.; Zhang, Q.; Deng, F.; Luo, X.; Dionysiou, D.D. Rapid toxicity elimination of organic pollutants by the photocatalysis of environment-friendly and magnetically recoverable step-scheme $SnFe_2O_4$/$ZnFe_2O_4$ nano-heterojunctions. *Chem. Eng. J.* **2020**, *379*, 122264. [CrossRef]
47. Ismael, M. Enhanced photocatalytic hydrogen production and degradation of organic pollutants from Fe (III) doped TiO_2 nanoparticles. *J. Environ. Chem. Eng.* **2020**, *8*, 103676. [CrossRef]
48. Shah, N.S.; Khan, J.A.; Sayed, M.; Khan, Z.U.H.; Rizwan, A.D.; Muhammad, N.; Boczkaj, G.; Murtaza, B.; Imran, M.; Khan, H.M.; et al. Solar light driven degradation of norfloxacin using as-synthesized Bi^{3+} and Fe^{2+} co-doped ZnO with the addition of HSO^{5-}: Toxicities and degradation pathways investigation. *Chem. Eng. J.* **2018**, *351*, 841–855. [CrossRef]
49. Boruah, P.K.; Sharma, B.; Karbhal, I.; Shelke, M.V.; Das, M.R. Ammonia-modified graphene sheets decorated with magnetic Fe3O4 nanoparticles for the photocatalytic and photo-Fenton degradation of phenolic compounds under sunlight irradiation. *J. Hazard. Mater.* **2017**, *325*, 90–100. [CrossRef]
50. Xu, T.; Ji, H.; Gu, Y.; Tong, T.; Xia, Y.; Zhang, L.; Zhao, D. Enhanced adsorption and photocatalytic degradation of perfluorooctanoic acid in water using iron (hydr)oxides/carbon sphere composite. *Chem. Eng. J.* **2020**, *388*, 124230. [CrossRef]
51. Feng, X.; Guo, H.; Patel, K.; Zhou, H.; Lou, X. High performance, recoverable Fe_3O_4ZnO nanoparticles for enhanced photocatalytic degradation of phenol. *Chem. Eng. J.* **2014**, *244*, 327–334. [CrossRef]
52. Rajabi, H.R.; Khani, O.; Shamsipur, M.; Vatanpour, V. High-performance pure and Fe^{3+}-ion doped ZnS quantum dots as green nanophotocatalysts for the removal of malachite green under UV-light irradiation. *J. Hazard. Mater.* **2013**, *250-251*, 370–378. [CrossRef] [PubMed]
53. Hassandoost, R.; Pouran, S.R.; Khataee, A.; Orooji, Y.; Joo, S.W. Hierarchically structured ternary heterojunctions based on Ce(3+)/Ce(4+) modified Fe3O4 nanoparticles anchored onto graphene oxide sheets as magnetic visible-light-active photocatalysts for decontamination of oxytetracycline. *J. Hazard. Mater.* **2019**, *376*, 200–211. [CrossRef] [PubMed]
54. Narouz, M.R.; Osten, K.M.; Unsworth, P.J.; Man, R.W.Y.; Salorinne, K.; Takano, S.; Tomihara, R.; Kaappa, S.; Malola, S.; Dinh, C.-T.; et al. N-heterocyclic carbene-functionalized magic-number gold nanoclusters. *Nat. Chem.* **2019**, *11*, 419–425. [CrossRef]
55. Shen, D.; Xu, Y.; Shi, S.-L. A Bulky Chiral N-Heterocyclic Carbene Palladium Catalyst Enables Highly Enantioselective Suzuki-Miyaura Cross-Coupling Reactions for the Synthesis of Biaryl Atropisomers. *J. Am. Chem. Soc.* **2019**, *141*, 14938–14945. [CrossRef]
56. Sau, S.C.; Hota, P.K.; Mandal, S.K.; Soleilhavoup, M.; Bertrand, G. Stable abnormal N-heterocyclic carbenes and their applications. *Chem. Soc. Rev.* **2020**, *49*, 1233–1252. [CrossRef]
57. Doddi, A.; Peters, M.; Tamm, M. N-Heterocyclic Carbene Adducts of Main Group Elements and Their Use as Ligands in Transition Metal Chemistry. *Chem. Rev.* **2019**, *119*, 6994–7112. [CrossRef]
58. Singha, S.; Patra, T.; Daniliuc, C.G.; Glorius, F. Highly Enantioselective 5+2 Annulations through Cooperative N-Heterocyclic Carbene (NHC) Organocatalysis and Palladium Catalysis. *J. Am. Chem. Soc.* **2018**, *140*, 3551–3554. [CrossRef]
59. Janssen-Mueller, D.; Schlepphorst, C.; Glorius, F. Privileged chiral N-heterocyclic carbene ligands for asymmetric transition-metal catalysis. *Chem. Soc. Rev.* **2017**, *46*, 4845–4854. [CrossRef]
60. Peris, E. Smart N-Heterocyclic Carbene Ligands in Catalysis. *Chem. Rev.* **2018**, *118*, 9988–10031. [CrossRef]
61. Froese, R.D.J.; Lombard, C.; Pompeo, M.; Rucker, R.P.; Organ, M.G. Designing Pd N-Heterocyclic Carbene Complexes for High, Reactivity and Selectivity for Cross-Coupling Applications. *Acc. Chem. Res.* **2017**, *50*, 2244–2253. [CrossRef]
62. Liang, Q.; Song, D. Iron N-heterocyclic carbene complexes in homogeneous catalysis. *Chem. Soc. Rev.* **2020**, *49*, 1209–1232. [CrossRef]
63. Kim, I.; Im, H.; Lee, H.; Hong, S. N-Heterocyclic carbene-catalyzed deaminative cross-coupling of aldehydes with Katritzky pyridinium salts. *Chem. Sci.* **2020**, *11*, 3192–3197. [CrossRef]
64. Jazzar, R.; Soleilhavoup, M.; Bertrand, G. Cyclic (Alkyl)- and (Aryl)-(amino)carbene Coinage Metal Complexes and Their Applications. *Chem. Rev.* **2020**, *120*, 4141–4168. [CrossRef] [PubMed]
65. Li, G.; Zhou, T.; Poater, A.; Cavallo, L.; Nolan, S.P.; Szostak, M. Buchwald-Hartwig cross-coupling of amides (transamidation) by selective N-C(O) cleavage mediated by air- and moisture-stable Pd(NHC)(allyl)Cl precatalysts: Catalyst evaluation and mechanism. *Catal. Sci. Technol.* **2020**, *10*, 710–716. [CrossRef]

66. Cao, Z.; Kim, D.; Hong, D.; Yu, Y.; Xu, J.; Lin, S.; Wen, X.; Nichols, E.M.; Jeong, K.; Reimer, J.A.; et al. A Molecular Surface Functionalization Approach to Tuning Nanoparticle Electrocatalysts for Carbon Dioxide Reduction. *J. Am. Chem. Soc.* **2016**, *138*, 8120–8125. [CrossRef]
67. Zhuang, Y.; Qian, Y.; Tu, D.; Li, Y.; Liu, J.; Shen, L.; Wu, D. NHC-Stabilized Inverse Crown Ethers Featuring the μ4-Oxo [Mg4O] Core. *Eur. J. Inorg. Chem.* **2021**, *2021*, 3420. [CrossRef]
68. Klaseboer, E.; Sun, Q.; Chan, D.Y.C. Nonsingular field-only surface integral equations for electromagnetic scattering. *IEEE Trans. Antennas Propag.* **2017**, *65*, 972–977. [CrossRef]
69. Sun, Q.; Klaseboer, E.; Chan, D.Y.C. Robust multiscale field-only formulation of electromagnetic scattering. *Phys. Rev. B* **2017**, *95*, 045137. [CrossRef]
70. Sun, Q.; Klaseboer, E.; Yuffa, A.J.; Chan, D.Y.C. Field-only surface integral equations: Scattering from a perfect electric conductor. *J. Opt. Soc. Am. A Opt. Image Sci. Vis.* **2020**, *37*, 276–283. [CrossRef] [PubMed]
71. Sun, Q.; Klaseboer, E.; Yuffa, A.J.; Chan, D.Y.C. Field-only surface integral equations: Scattering from a dielectric body. *J. Opt. Soc. Am. A Opt. Image Sci. Vis.* **2020**, *37*, 284–293. [CrossRef] [PubMed]
72. Querry, M.R. *Optical Constants*; Contractor Report; SAO/NASA Astrophysics Data System: Cambridge, MA, USA, 1985.
73. Huang, Y.; Ning, L.; Feng, Z.; Ma, G.; Yang, S.; Su, Y.; Hong, Y.; Wang, H.; Peng, L.; Li, J. Graphitic carbon nitride nanosheets with low ON1-doping content as efficient photocatalysts for organic pollutant degradation. *Environ. Sci. Nano* **2021**, *8*, 460–469. [CrossRef]